

Dust Concentration at the Boundary Between Steady Super/Sub-Keplerian Flow Created by Inhomogeneous Growth of MRI

M. T. Kato

*Department of Earth and Planetary Science, Tokyo Institute of Technology, Ookayama
2-1-12-I2-10, Meguro-ku, Tokyo*

marikok@geo.titech.ac.jp

M. Fujimoto

*Institute of Space and Astronomical Science, Japan Aerospace Exploration Agency,
Yoshinodai 3-1-1, Sagamihara, Kanagawa*

and

S. Ida

*Department of Earth and Planetary Science, Tokyo Institute of Technology, Ookayama
2-1-12-I2-10, Meguro-ku, Tokyo*

ABSTRACT

How to create planetesimals from tiny dust particles in a proto-planetary disk before the dust particles spiral to the central star is one of the most challenging problems in the theory of planetary system formation. In our previous paper (Kato et al. 2009), we have shown that a steady angular velocity profile that consists of both super and sub-Keplerian regions is created in the disk through non-uniform excitation of Magneto-Rotational Instability (MRI). Such non-uniform MRI excitation is reasonably expected in a part of disks with relatively low ionization degree. In this paper, we show through three-dimensional resistive MHD simulations with test particles that this radial structure of the angular velocity indeed leads to prevention of spiral-in of dust particles and furthermore to their accumulation at the boundary of super-Keplerian and sub-Keplerian regions. Treating dust particles as test particles, their motions under the influence of the non-uniform MRI through gas drag are simulated. In the most favorable cases (meter-size dust particles in the disk region with a relatively large fraction of MRI-stable region), we found that the dust concentration is peaked around

the super/sub-Keplerian flow boundary and the peak dust density is 10,000 times as high as the initial value. The peak density is high enough for the subsequent gravitational instability to set in, suggesting a possible route to planetesimal formation via non-uniformly excited MRI in weakly ionized regions of a disk.

Subject headings: protoplanetary disks — instabilities — MHD — planetary systems: formation — turbulence

1. Introduction

One of the most serious problems in planet formation is how the dust components grow up to larger objects in protoplanetary disks. The known key-stage is when the dust particles are meter-size (Adachi 1976; Weidenschilling 1977). Since gas pressure gradient in a protoplanetary disk is negative, gas rotates at sub-Keplerian velocity. On the other hand, the dust particles tend to rotate at Keplerian velocity and therefore they feel headwind of gas. Losing their angular momenta, they spiral into a central star quickly on timescales of 100 years.

One possibility to overcome the meter-size barrier is the planetesimal formation via gravitational collapse of a cluster composed with small dust particles (Safronov 1969; Goldreich & Ward 1973). The dust would settle to midplane in the absence of turbulence. Early studies of dust settling in turbulent accretion disks were carried out by Cuzzi et al. (1993), Miyake & Nakagawa (1995) and Dubrulle et al. (1995). They presented that large dust particles settle down toward their equilibrium distribution in a turbulent diffusive time scale while small ones remain mixed throughout the whole gas disk. If dust density in midplane becomes high enough, Kelvin-Helmholtz instabilities between a sediment layer of dust and the overlying gas can drive turbulence and mix the dust layer enough to prevent gravitational instability (Weidenschilling 1977, 1980; Ishitsu & Sekiya 2003; Gomez & Ostriker 2005). Johansen et al. (2006b), however, carried out two-dimensional simulation and found active turbulent concentration. Except the effect of Kelvin-Helmholtz instabilities, the high dust density in midplane leads to a streaming instability (Goodman & Pindor 2000; Youdin & Goodman 2005) because the dust is susceptible to preferential radial migration relative to the gas (Nakagawa et al. 1986). The streaming instability was shown to lead to turbulence and concentrate dust particles locally (Youdin & Johansen 2007; Johansen & Youdin 2007). As one of other mechanisms of turbulent concentration, the effect of the turbulence driven by the magnetorotational instability (MRI; Balbus & Hawley 1991; Hawley et al. 1995) is recognized. Planetesimal formation by gravitational instability in the MRI turbulence is addressed by Johansen et al. (2006a, 2007) and Balsara et al. (2009).

Turbulence level is the most fundamental parameter governing whether planetesimals can form by gravitational instability in these models. The turbulence level of MRI depends on the ionization degree of disk gas and the strength of magnetic field. The linear analysis showed that the growth rate of MRI is reduced by ohmic diffusion when collisions are so frequent that not only the ions and neutrals are well coupled but also electrical currents are damped (Jin 1996; Sano & Miyama 1999). At the same time, the growth wavelength becomes longer and transport rate of angular momentum is diminished. The nonlinear evolution of the MRI in nonideal MHD starting from the weak vertical magnetic field has been studied by Sano et al. (1998). They found that sustained MHD turbulence requires the magnetic Reynolds number $R_m = v_A^2/\eta\Omega \gtrsim 1.0$, where v_A , η and Ω are Alfvén velocity, magnetic resistivity and Keplerian rotation frequency.

The values of η are regulated by an ionization structure in a protoplanetary disk. The inner regions of a disk are thermally ionized (Pneuman & Mitchell 1965; Umebayashi 1983). At greater distances from the disk center, stellar X-rays and diffuse cosmic rays ionize the surface gas layer down to a certain column density (Glassgold et al. 1997; Igea & Glassgold 1999). In moderately distant regions in which disk column density is high enough, midplane layers are not highly ionized and MRI could be inactive there. This region is called "dead zone" (Gammie 1996).

The characteristics and interesting physics are prospective around dead zones. The magnetic turbulence outside the dead zone, which transports angular momentum and mass, creates gas density bump at the outer boundary of the dead zone. This density pile-up triggers the Rossby wave (Li et al. 2001; Varniere & Tagger 2006) to form long-life anticyclonic vortices. Barge & Sommeria (1995) suggested that the dust particles are trapped in a center of vortex. By numerical simulation of Rossby vortices including solid particles, Inaba & Barge (2006) confirmed the enhancement of dust density there. Lyra et al. (2008) showed that gravitationally bound embryos can form in the regions of enhanced dust density.

Kato et al. (2009, ; hereafter referred to as Paper I) showed that non-uniform excitation of MRI creates angular velocity profile that consists of super and sub-Keplerian regions locally in the disk (for details, see section 2). It is expected that this radial structure of the angular velocity leads to prevention of spiral-in of dust particles and their accumulation at the boundary of super and sub-Keplerian regions, since the super-Keplerian flow pushes the dust particles outward while the sub-Keplerian flow drags them inward. This interesting mechanism is based on the co-existence of MRI active and inactive regions. The ionization degree that regulates MRI depends on the relative abundance and size distribution of grains (Wardle & Ng 1999; Sano et al. 2000). It can also be changed by phase chemistry (Ilgner & Nelson 2008). Slight changes in these quantities near boundaries at global ac-

tive/dead zones of MRI may create the local inhomogeneity in MRI growth. We will address this issue in a subsequent paper. Note that the local model in this paper is not a toy model that mimics the global inhomogeneous structure of dead and active zones.

In this paper, we investigate dust accumulation induced by inhomogeneous MRI evolution by three-dimensional non-ideal MHD simulation including dust particles. The dust particles are represented by Lagrangian particles suffering gas drag and are assumed not to affect on gas. We consider both cases with radially non-uniform magnetic resistivity under uniform magnetic field direction and non-uniform magnetic field with radially uniform magnetic resistivity. MRI develops in low resistivity regions in the former case and in strong vertical magnetic field regions in the latter case. The latter model is the same as the model adopted in Paper I. We briefly summarize the results of Paper I in section 2. We explain our simulation setting in section 3. In section 4, we present that the MRI leads to quasi-steady state and particles are locally concentrated as expected. We also analyze the distributions of particle radial velocity to understand the effect of weak remnant magnetic turbulence. We examine how high the particle density enhancement is and the possibility of planetesimal formation via gravitational instability. Finally, we summarize our results and discuss their implications in section 5.

2. Brief Summary of Paper I

In Paper I, we have studied how the angular velocity profile of gas is modified when MRI is excited non-uniformly in a part of a disk. Local two-dimensional simulations (in the x - z plane where x and z are radial and vertical coordinates to the disk) with the shearing box boundary conditions were performed. We assumed the ionization degree of the gas to be relatively low. The vertical component to the disk plane (z component) of magnetic field was changed along the radial direction (x) while the absolute values of the field is constant. In the part of a disk where the ionization degree is low (equivalently, resistivity is high), MRI is active only in the regions with relatively large vertical component of the magnetic field. One of the models used in the present paper has the same setting but with three-dimensional simulations, while the other model in the present paper assumes non-uniform resistivity with uniform magnetic field.

The most illustrative result of Paper I is shown in Figure 1. Time evolution ($t\Omega = 0, 40, 70$) of vertically averaged pressure and angular velocity of gas is plotted in Panels a and b. MRI is excited only in the initially unstable region ($-0.71 < x/H < 0.71$) with large enough initial vertical field and vigorous angular momentum and mass transport occurs within the unstable zone. When the magnetic perturbations are propagated to the initially

stable regions ($|x/H| < 0.71$), they are dissipated via resistivity and the large part of the stable region remains undisturbed. Hereafter, we call the initially MRI stable and unstable regions simply as "stable" and "unstable" regions, respectively. After the vigorous angular momentum and mass transfer, a new quasi-steady state with the local rigid rotation feature appears in the unstable region (Figure 1b). The pressure profile of the gas is also modulated (Figure 1a). The rigid rotation feature that appears in the saturated quasi-steady state is sustained by the modified pressure pattern with its two peaks located around the unstable-stable boundary regions and its bottom located in the middle of the unstable zone. The quasi-steady rigid rotation pattern results in super-Keplerian angular velocity at the outer part of the unstable region. Since the gas in the stable region is unperturbed and remains sub-Keplerian when the global pressure gradient is taken into account, one finds that super- and sub-Keplerian zones co-exist in the part of the disk due to the non-uniform excitation of MRI.

The co-existence of super- and sub-Keplerian zones has significant implication for the dust particle dynamics in a disk. As mentioned in the Introduction, the dust particles feel headwind and migrate inward in the sub-Keplerian gas flow. On the other hand, the dust particles feel tailwind and migrate outward in the super-Keplerian zone. Then at a boundary between sub- and super-Keplerian zones, with the super-Keplerian zone situated on the inner side, which is indeed seen at the outer edge of the unstable region, the inward migration of dust particles through the sub-Keplerian zone (the stable zone) are halted. The boundary region potentially acts as a barrier for the dust infall and furthermore as the focal annulus of the dust particle concentration which may eventually lead to planetesimal formation.

The widths of the stable and unstable regions are one of the key parameters that determine the characteristics of the final state. We have found that the final state is classified by the spatially averaged magnetic Reynolds number in the initial condition,

$$R_{\text{m,ave}} = v_{\text{Az,ave}}^2 / \eta \Omega, \quad (1)$$

where $v_{\text{Az}} = B_z / \sqrt{4\pi\rho}$ is z component of Alfvén velocity. If $R_{\text{m,ave}}$ is less than unity, a quasi-steady state with the local super-Keplerian rotation appears. The turbulence level within the stable region and at the boundary varies according to $R_{\text{m,ave}}$. The degree of dust concentration at the boundary region would be affected by the level of turbulence. For $R_{\text{m,ave}} > 1$, the magnetic perturbations are not dissipated enough within the stable region and the velocity pattern undergoes perpetual changes without reaching a quasi-steady state. Steady accumulation of dust particles is not expected in this case. Note that our simulations with constant $R_{\text{m,ave}}$ converge with increasing resolution, because the resistivity η (ohmic dissipation) is explicitly included in our simulations and it is kept constant due to the constancy of $R_{\text{m,ave}}$.

In the present paper, we address the following questions that arise from the results of Paper I: (1) Do dust particles truly concentrate at the boundary? (2) Is the emergence of the quasi-steady rigid rotation region preserved in three-dimensional cases? (3) How does remaining weak turbulence affect the dust concentration process? (4) Are dust particles concentrated dense enough on long enough timescales for subsequent gravitational instability to set in?

3. Model

3.1. Equations

Here we are concerned with a small region in a protoplanetary disk and study the local dynamics of gas and dust particles. The gas motion is calculated by resistive MHD simulations. The dust particles are modeled as test particles that move under the effects of the gravity from the central star and the gas drag.

We adopt a local shearing box that has radial (x), azimuthal (y) and vertical (z) directions. The boundary conditions are periodic in the y and z directions and the shearing box boundary condition is used in the x direction (Wisdom & Tremaine 1988; Hawley et al. 1995). We calculate compressible resistive magnetohydrodynamic (MHD) equations given by

$$\frac{\partial \mathbf{u}}{\partial t} + (\mathbf{u} \cdot \nabla) \mathbf{u} = -\frac{1}{\rho} \nabla \left(P + \frac{\mathbf{B}^2}{8\pi} \right) + \frac{1}{4\pi\rho} (\mathbf{B} \cdot \nabla) \mathbf{B} - 2\boldsymbol{\Omega} \times \mathbf{u} + 3\Omega^2 x \hat{\mathbf{x}} - \beta c_s \Omega \hat{\mathbf{x}}, \quad (2)$$

$$\frac{\partial \rho}{\partial t} + \nabla \cdot (\rho \mathbf{u}) = 0, \quad (3)$$

$$\frac{\partial \mathbf{B}}{\partial t} = \nabla \times [(\mathbf{u} \times \mathbf{B}) - \eta (\nabla \times \mathbf{B})], \quad (4)$$

$$P = c_s^2 \rho, \quad (5)$$

where $\hat{\mathbf{x}}$ is a unit vector in the x direction. We consider only the Ohmic dissipation in equation (4) because influence of ambipolar diffusion is negligible at the density level that is expected in the inner ($\lesssim 100$ AU) midplane of a protoplanetary disk (Jin 1996; Sano & Miyama 1999; Chiang & Murray-Clay 2007). The last terms in r.h.s. of equation (2) allows the effect of the global pressure gradient to be taken into account in our local model. The parameter β is related to the global pressure gradient as

$$-\frac{1}{\rho} \frac{\partial P}{\partial r} = -\frac{1}{\rho} \left(\frac{P}{r} \right) \alpha \quad (6)$$

– 7 –

$$= -\frac{H}{r}\alpha c_s \Omega \quad (7)$$

$$= -\beta c_s \Omega \left(= -\frac{\beta^2}{\alpha} \Omega^2 r \right), \quad (8)$$

where we assume $P \propto r^\alpha$, with constant α and an isothermal disk $c_s = H\Omega$, where H is disk scale height. The value of $\beta (= \alpha H/r = \alpha c_s/r\Omega)$ is treated as a constant parameter in our local model. We solve equation (4) with MOCCT method (Stone & Norman 1992) and the advection terms in equation (2) with CIP method (Yabe & Aoki 1991).

The dust grains are treated as test particles. The equation of motion of the i -th particle is given by

$$\frac{d\mathbf{v}_i}{dt} = -2\mathbf{\Omega} \times \mathbf{v}_i + 3\Omega^2 x_i \hat{\mathbf{x}} - \frac{1}{\tau_f} (\mathbf{v}_i - \mathbf{w}_i), \quad (9)$$

where \mathbf{w}_i is the gas velocity at the location of the i -th particle, which is interpolated with the three-dimensional first-order interpolation scheme by values of \mathbf{u} at the eight grid points surrounding the particle.

The friction force, the last term in equation (9), is proportional to the velocity difference between the dust and gas since the dust sizes that we are concerned with are in Epstein and Stokes drag-law regimes. The characteristic friction (stopping) timescale τ_f is given by

$$\tau_f = \frac{a_\bullet^2 \rho_\bullet}{\min(a_\bullet c_s, 9/2\nu) \rho}, \quad (10)$$

where a_\bullet , ρ_\bullet and c_s are the dust particle radius, dust particle density and the sound speed, respectively. ν is the molecular viscosity and equal to $c_s \lambda/2$, where λ is the mean free path of the gas molecules. Depending on the particle size relative to the mean free path ($a_\bullet >$ or $< (9/4)\lambda$) the drag law changes from the Epstein to the Stokes regime. The scaled friction times of $\tau_f \Omega = 0.1$ and 1.0 correspond to the grain sizes of approximately 0.1 and 1 meter, respectively, at the radial location of Jupiter in the minimum mass solar nebula model.

3.2. Initial Setup

All of our simulations start with uniform gas density (ρ_0) and gas pressure (P_0). The global gas pressure gradient is set to be $\beta = -0.04$. The initial gas angular velocity profile is given by unperturbed Keplerian flow $-(3/2)x\Omega$ and a small reduction due to global gas pressure gradient ($\beta c_s/2$), $u_y = -(3/2)x\Omega + \beta c_s/2$. Initial disturbances are given to the gas

radial velocity with the amplitude $|\delta u_x| = 0.001c_s$. Test particles are initially orbiting at the Kepler angular velocity. The particles move inward in the initial stage because they lose their angular momentum by the headwind that they feel due to the global pressure gradient. This is the dust infall problem described in Introduction. Initially 8 particles per grid are distributed. Since typical grid we use is $(250 - 950) \times 100 \times 50$ (Table 1), totally $\sim O(10^7)$ particles are distributed.

The non-uniformity in the MRI growth is set either by non-uniform resistivity (CASE1) or non-uniform vertical (z) component of the magnetic field (CASE2). We describe these cases in details in the following.

3.2.1. CASE1

In CASE1, gas ionization degree is set to be radially inhomogeneous under the uniform magnetic field. The linear analysis for MRI caused by vertical magnetic field shows that the larger resistivity makes unstable wavelength longer (Jin 1996; Sano & Miyama 1999). The upper limit to the wavelength, $\lambda_{z,\text{crit}}$, is scale height for actual disks while in our simulation, it is the size of the simulation box in the z direction (L_z). The critical value of resistivity with which the modes with wavelength shorter than $\lambda_{z,\text{crit}}$ cannot grow is

$$\eta_{\text{crit}} \simeq \frac{1}{k_{z,\text{crit}}} \sqrt{\frac{2}{\beta_{\text{plasma}}} \left(\frac{3\Omega^2}{c_s^2} - \frac{2k_{z,\text{crit}}^2}{\beta_{\text{plasma}}} \right)} H^2 \Omega, \quad (11)$$

where $k_{z,\text{crit}}$ is the wave number corresponding $\lambda_{z,\text{crit}}$. Here $\beta_{\text{plasma}} = 2c_s^2/v_{\text{Az}}^2$ is the plasma beta. In our case there is no growing mode if the resistivity makes $\lambda_{z,\text{crit}}$ larger than L_z .

In CASE1, we set $\beta_{\text{plasma}} = 4000$ and $\mathbf{B}_0 = (0, 0, B_z)$. Resistivity varies in the radial direction such that MRI grows only in a limited zone in the center of the simulation box. The resistivity distribution is not changed throughout runs. The radial distribution is shown in Figure 2a. In this paper, the zone at the center where resistivity is initially sub-critical is referred to as the "unstable" region. The radial width of the stable and unstable regions are denoted by L_s and L_u , respectively.

We have performed only one simulation run for CASE1, which will be called model- η in the later sections. Table 1 lists the parameter values used in the run.

3.2.2. CASE2

The set-up of CASE2 is the same as that in Paper I except for three-dimensional simulations. The magnetic resistivity is uniform but the vertical component of magnetic field varies in the radial direction. That is, the initial magnetic field is situated as $\mathbf{B}_0 = (0, B_0 \sin \theta, B_0 \cos \theta)$, where $\theta = \theta(x)$ is the angle between the vertical axis and the magnetic field. The vertical magnetic component, or θ , determines whether the instability grows or not. For large θ , vertical magnetic field is weak and short vertical wavelength modes grow faster. Since such modes are dissipated by the ohmic dissipation effectively, the vertical field MRI does not develop. The MRI caused by the azimuthal magnetic field is known to grow rapidly with the limit of extremely short vertical wavelength in ideal MHD (Balbus & Hawley 1998) but the such short vertical wavelength modes tend to be damped resistively. In fact, Papaloizou & Terquem (1997) found that the azimuthal field MRI growth ceases for the ionization degree higher than that stabilizes the vertical field MRI. We also did not find the development of the azimuthal field MRI in our simulation as long as the box size in the y direction is expanded by a factor up to 3 from the nominal cases at least for about 20 orbits in which the gas velocity and dust density vary dramatically.

The radial distribution of θ is shown in Figure 2b. Here, $\beta_{plasma} = 400$, and the magnetic resistivity is $\eta = 0.002H^2\Omega$. The larger vertical magnetic component in the center of the box makes MRI locally unstable. Outside the unstable zone the value of θ is smaller than the critical one and MRI is stabilized.

The two-dimensional version of CASE2 was studied in Paper I, in which we found that if the spatially averaged magnetic Reynolds number $R_{m,ave}$ (Equation (1)) is small enough, the quasi-steady angular velocity profile that is deviated significantly from the Keplerian is generated. Since it is expected that this feature is preserved in three dimensional simulations and $R_{m,ave}$ depends on the radial widths of the unstable region L_u and the stable region L_s , we investigate several cases with various L_s while keeping $L_u = 1.4H$ in CASE2: $L_s = 4.0H$ ($R_{m,ave} = 0.096$, model-s40), $1.1H$ ($R_{m,ave} = 0.37$, model-s11), $0.55H$ ($R_{m,ave} = 0.64$, model-s055). Note that two-dimensional calculations with the same L_s and L_u were performed in Paper I.

In all of these cases, the friction time is set to be $1.0/\Omega$. To investigate the effects of the friction time, we set it to be $0.1/\Omega$ in model-t01, which has $L_u = 1.4H$ and $L_s = 4.0H$ (the same as model-s40). The initial settings are summarized in Table 1.

3.3. Estimation of Particle Drift Speed

When the condition $R_{\text{m,ave}} < 1$ is met, the non-uniform growth of MRI will create a new quasi-steady gas angular flow pattern that should affect the dust particle dynamics substantially (Paper I). At the same time, weak remnant turbulent flow may be superposed upon the quasi-steady pattern and would affect the dust motions, with its degree being dependent on the spatially averaged magnetic Reynolds number. Here we evaluate these two effects on the dust accumulation. We will be focusing on the x component of the dust velocities v_x .

If the turbulence is small enough, as we have mentioned in section 2, the velocity difference in the y component (angular velocity) between dust and gas is the determining factor for the assemblage of dust particles at the boundary between super and sub-Keplerian zones. In order to quantitatively analyze the effect of the remnant turbulence, we divide the radial component of the particle velocity into two components: one is that due to the non-Keplerian gas motion in the quasi-steady state achieved at the MRI saturation and the other is that due to turbulence. The equation of motion for the dust velocity field at the grid point is

$$\frac{d\mathbf{v}}{dt} = -2\boldsymbol{\Omega} \times \mathbf{v} + 3\Omega^2 x \hat{\mathbf{x}} - \frac{1}{\tau_f} (\mathbf{v} - \mathbf{u}). \quad (12)$$

We set $\mathbf{v} = \mathbf{v}' + v_{\text{kep}} = \mathbf{v}' - (3/2)x\Omega\hat{\mathbf{y}}$ where \mathbf{v}' is a deviation from Kepler flow. Assuming $d\mathbf{v}'/dt = 0$ ($d\mathbf{v}/dt = -(3/2)\Omega\hat{\mathbf{y}}$) in x and y components and eliminating v'_y , the x component of the particle velocity is given by

$$\begin{aligned} v_x \sim v_d &= \frac{2\delta u_y}{\tau_f \Omega + (\tau_f \Omega)^{-1}} + \frac{u_x}{(\tau_f \Omega)^2 + 1} \\ &= v_f + v_t, \end{aligned} \quad (13)$$

where δu_y is the gas angular velocity relative to Keplerian velocity, $\delta u_y = u_y - v_{\text{kep}}$ and u_x is the gas radial velocity due to turbulent viscosity. The component v_f represents the particle velocity due to non-Keplerian gas motion in the quasi-steady state, because it does not vanish even in the non-turbulence case, $u_x = 0$. Although turbulence also contributes to v_f , the contribution due to turbulence can be neglected compared with that due to the quasi-steady non-Keplerian gas flow, except for strong turbulence case where the quasi-steady flow is not achieved. As we will show below, the component v_t can be regarded as characteristic amplitude of the velocity dragged by turbulence, although v_t changes with time due to the temporal change of v_x and the assumption of $d\mathbf{v}'/dt = 0$ is no more valid in the turbulent case.

Later in this paper, v_f and v_t will be calculated by equation (13), using gas velocity obtained by the MHD simulation, and they will be presented as a function of x after azimuthal and vertical averaging. The ratio of the absolute values of the two is

$$\frac{|v_t|}{|v_f|} = \frac{|u_x|}{2|\delta u_y|} \frac{1}{\tau_f \Omega}. \quad (14)$$

The turbulence effect is indicated by this ratio. It is stronger, if i) turbulent flow is larger than the angular velocity difference δu_y , and/or ii) the dust size (τ_f) is smaller. In the annulus where dust particles are expected to accumulate, $\delta u_y \simeq 0$ and the ratio diverges. However, we will show below that this divergence is restricted only in narrow regions and the effect of turbulence does not prevent dust accumulation.

We have set the global gas pressure gradient to be $\beta = -0.04$ so that a direct comparison with the result by Johansen et al. (2007) could be performed. This global pressure gradient, however, is less steep than in the Minimum Mass Solar Nebular model (Hayashi 1981). A steeper global pressure gradient ($\beta < -0.04$) has at least three effects in the current context: (1) The baseline of gas velocity becomes lower than the Keplerian velocity and it becomes more difficult to create super-Keplerian regions whose outer-edges accumulate the dust particles. (2) If a super-Keplerian region appears, accumulation towards its outer-edge is faster (v_f is faster) for steeper pressure gradient. This has a positive impact on the dust accumulation efficiency. (3) The outer-edge of super-Keplerian region would change its location according to the value of β . The turbulence level at the focal annulus of dust accumulation varies accordingly. If the turbulence level is higher, it by itself has a negative impact. In CASE2, we have also carried out the runs with $\beta = -0.10$ and found that the trapping of dust particles does occur and its efficiency is slightly higher.

4. Result

4.1. Result of CASE1

In the model- η , the non-uniform excitation of MRI is realized by non-uniform resistivity while the magnetic field is set uniform. The result of model- η nicely illustrates our scenario for dust accumulation.

Figure 3a shows the evolution of MRI. The black lines depict the magnetic field lines and the gray scale shows the gas radial velocity. The unstable region lies between two white lines ($|x/H| = 0.18$). MRI is first excited only in the initially unstable region (see the plot at $t\Omega = 19$) and significant angular momentum and mass are transported there. The MRI turbulence intrudes into the stable region ($t\Omega = 30$). Deep inside the stable

region, however, is always undisturbed ($|x/H| \gtrsim 0.5$) because of the rapid dissipation by the enhanced resistivity.

Figures 4a and 4b show the radial profiles of the pressure and the angular velocity of the gas, respectively. The quantities have been averaged azimuthally and vertically. The sampling times are $t\Omega = 0, 40$, and 70 . The zone between the two vertical dotted lines is the unstable region. The inhomogeneous MRI growth creates the rigid rotation pattern in the middle of the simulation box ($|x/H| \lesssim 0.15$). The pressure distribution is considerably modified such that the resultant pressure gradient force balances with the modified Coriolis force. The flattened rotation profile cannot sustain the excitation of MRI in the unstable zone. Indeed, the turbulence weakens extremely at $t\Omega = 70$ in Figure 3a. The profiles of pressure or angular velocity in Figures 4a and 4b depict the quasi-steady state set up by the non-uniform MRI activity. Most of what we see here is quite similar to the results of the two-dimensional simulations described in Paper I even though the initial settings for seed magnetic field and resistivity distribution are totally different.

The rigid rotation causes gas to rotate faster than Keplerian velocity in $0.0 \lesssim x/H \lesssim 0.4$ (Figure 4b). This can change the particle migration drastically. Figure 3b shows the temporal evolution of the particle density. The color code is set such that the maximum is ten times the initial value. After the particles are swept out of the unstable region by the MRI flow, they accumulate to the location at $x/H \simeq 0.4$ (note that particles leaving the simulation box from the left hand boundary reenter from the right hand boundary after the shearing box correction is taken into account). Though not visible in the panels, the particles initially in the stable zone are swept likewise towards the same location. The accumulation of particles is most clearly shown in Figure 4c in which the radial distribution of the number of particles that is averaged azimuthally and vertically and is normalized by the initial value.

To analyze the particle concentration dynamics in more details, in Figure 4d, we plot the maximum (the solid line) and the minimum (the dashed line) values of v_f at a given x . The radial velocities of particles are predicted by equation (13) using simulated gas velocity after the establishment of the quasi-steady flow ($t\Omega = 70$). Since the gas velocity is influenced by remnant turbulence, which has variations dependent on y and z , the predicted radial velocities have the maximums and the minimums. Figure 4d shows that the turbulent fluctuations are sufficiently small compared with the systematic angular velocity change due to the modulation of the pressure profile. In Figure 4d, the max/min of radial amplitude of turbulent velocity, v_t , is plotted. The amount of v_t is smaller than those of v_f except in the region $|v_f| \approx 0$. Thus, v_f represents the typical radial velocity of particles that is induced by head/tail angular wind in the absence of turbulence. Also plotted by dots are the actual particle radial velocities in the simulation result, v_x , which are concentrated near

the super/sub-Keplerian boundary. The data are taken at $t\Omega = 70$, but it stays essentially the same after the MRI saturation at $t\Omega \simeq 40$. In the radial regions where the maximum v_f is negative, gas rotation is sub-Keplerian for all y and z . In such radial locations, all the particles lose their angular momentum by the drag due to the slower angular wind and migrate inward. Conversely, in the regions where the minimum v_f is positive, all the particles migrate outward. In the middle of the stable zone ($|x/H| \gtrsim 0.5$), the gas flow is hardly changed. The value of $v_f \sim -0.02c_s$ corresponds to the infall speed due to global pressure gradient under the initial condition.

The particles are concentrated to the zone where both $\min[v_f] < 0$ and $\max[v_f] > 0$ are satisfied, which is situated around $x/H \sim 0.4$. The zone satisfying the two inequalities is rather narrow in x , and the difference between the maximum and the minimum v_f in this zone is small, resulting in high concentration of the dust particles at the outer-edge of the super-Keplerian zone as shown in Figure 4c. Because $|v_t/(v_f + v_t)| \ll 1$ in most of the regions except for the dust concentration zone, and the width of the dust concentration zone is small, the effects of turbulence do not significantly expand the dust concentration zone.

In Figure 5a, we plot the time variation of the maximum number of particles per grid. The more or less monotonic increase leads to the peak density of more than 1,000 times the initial density for $t\Omega \gtrsim 50$. We will show that the same clump grows in density while keeping its identity, which is needed for subsequent gravitational instability.

We pick up a particular time t_c during the period when the number of dust particles in the densest grid in the whole region increase monotonically or is saturated. Then, we search for the cell which has the largest number of particles in it. This cell is identified as the center of the most prominent clump that is composed of a number of cells. The ID numbers of the N_c particles in this cell of the highest density at $t = t_c$ are recorded and their motions are traced in time (also backward in time if necessary). To determine a new position of the center of the same clump at different times, we inspect the cells within 5 grid distance ($0.05H$) from the center of mass of the traced particles. The cell having the largest number of particles among them is defined to be the new position of the center of the clump. Table 2 shows t_c and N_c for the runs described in this paper. The time evolution of the number of particles in the cell at the center of the traced clump is plotted by the dotted lines in Figure 5a. It agrees with the maximum number of particles over the whole region, indicating that the same clump keeps its identity and stays to be the most prominent clump.

Another way to confirm that the clump steadily holds together is to inspect the velocity dispersion of particles. Figure 5b presents the velocity dispersion of particles as a function of distance from the center of the clump at $t = t_c$. All the compositional velocity dispersions are extremely low ($\lesssim 0.5\text{m/s}$), indicating that the particles are not to be diffused significantly.

When the self-gravity is taken into account, the high mass density and the low velocity dispersion should be the preferable condition for the subsequent planetesimal formation via gravitational instability.

When the global pressure gradient is steeper, the effects on dust dynamics described at the final part of Section 3 must be considered. For the case shown here, we make discussion by inspecting Figure 4d and equation (13). From the maximum amplitude of $\min[v_f]$ change ($\sim 0.08c_s$), we can expect that the value of $\min[v_f]$ remains positive (vertically and azimuthally uniform super-Keplerian region survives) if $\beta > -0.16$. That is, dust particles are prevented from infall as long as $\beta > -0.16$. This condition would be marginally satisfied at $r \lesssim 5\text{AU}$ in the MMSN model. Though the dust concentration that occurs at $v_f \simeq 0$ would be shifted inward with the more downward shift of the v_f (larger negative β), the turbulence effect on dust concentration would not change because the turbulence level v_t is evenly low. Therefore, with a steeper global pressure within the range of $\beta > -0.16$, the dust particles would drift faster towards and accumulate more efficiently at the outer-edge of super-Keplerian region.

4.2. Result of CASE2

In the models of CASE2, the non-uniform excitation of MRI is realized by non-uniform distribution of the magnetic field while resistivity is set uniform. In the presence of the substantial dissipation, the variation of the vertical component of the magnetic field switches the MRI condition from stable to unstable. In CASE2, the magnetic field angle is varied along the x (radial) direction such that MRI unstable region is situated only in the middle of the simulation box. The overall MHD dynamics varies according to the spatially averaged magnetic Reynolds number ($R_{m,\text{ave}}$) which is controlled by the width of the unstable/stable regions in the simulation box, as shown in Paper I. Here, the rotation pattern of the magnetic field and the width of the unstable region ($L_u = 1.4H$) is fixed.

4.2.1. model-s40

In the model-s40, the radial width of initial stable region L_s is $4.0H$. The relatively wide stable region results in $R_{m,\text{ave}} = 0.096 (\ll 1)$, which ensures effective enough dissipation to realize the quasi-steady state. Figure 6a presents the evolution of MRI in model-s40. The gray scale and lines are radial velocity of gas and magnetic field lines, respectively. The boundaries between the stable and unstable regions are depicted by the two white lines ($|x/H| \simeq 0.7$). It is found that the results of the present three-dimensional run are similar

to the corresponding two-dimensional results described in Paper I. The instability is excited only inside the unstable region. A part of the stable area is disturbed as well, because the resistivity is not large enough to dissipate the fluctuations immediately ($t\Omega = 35$). They are, however, eventually dissipated ($t\Omega = 40$ and 80).

Figure 7 presents radial distributions of pressure and angular velocity of gas, and the vertical component of the magnetic field. All the quantities obtained at $t\Omega = 0, 40$ and 70 , are averaged both azimuthally and vertically. The inhomogeneous MRI growth creates the near-rigid rotation pattern in the middle ($|x/H| \lesssim 0.6$) and the modified Coriolis force balances with the newly created pressure gradient force. The small vertical magnetic field together with the flat angular velocity profile suppresses the growth of MRI at later times inside the unstable region in which MRI was initially excited.

While these results of model-s40 are similar to those of model- η (CASE1), three differences are pointed out: i) The pressure and angular velocity are distributed less smoothly in the stable region in Figures 7a and 7b, which is attributed to deeper penetration of the MRI activity, ii) super-Keplerian region exists at $x/H \simeq -2.5$, in addition to the middle region of $0.0 \lesssim x/H \lesssim 2.0$, and iii) the weak instability persists at least until $t\Omega = 90$ in the stable region near the unstable region (Figure 6a). The super-Keplerian region at $x/H \simeq -2.5$ arises, because larger stable region makes mass and angular momentum transport less efficient around the middle of the stable region ($x/H \sim \pm 4.5$). As a result, the pressure gradient becomes positive at $x/H \simeq -2.5$. In model- η , the large magnetic resistivity in the stable region suppresses the instability even in the region of steep radial gradient of angular velocity. But, since in the models of CASE2, constant magnetic resistivity is assumed, the magnetic field is not completely dissipated in the stable region with the steep radial gradient.

Figure 6b presents the temporal evolution of the particle density. The evolution of the particle density pattern is similar to CASE1. However, unlike CASE1, not all the particles are assembled to the focal annulus. Figure 8a shows the azimuthally and vertically averaged value of the number of particles as a function of x . As expected, particles are condensed at $x/H \simeq 2.0$ (the outer-edge of the super-Keplerian region). Figure 8a also shows some other peaks in the stable region, which reflects the characteristics i) and ii) of the flow pattern described above.

Figure 8b shows radial velocities of particles predicted by equation (13) using simulated gas velocity after the establishment of the quasi-steady flow ($t\Omega = 70$). The dots concentrated at $x/H \simeq 2.0$ in the figure are actual velocities of all the simulated particles. The actual data of the particle velocities are well reproduced by equation (13), since most of the data points are located between the predicted minimum and maximum values. We further decompose v_d into v_f and v_t according to equation (13). Figure 8c presents the radial distri-

bution of the two components. The maximum and minimum values for each component are plotted. It is shown that the effect of the remnant turbulence is small and overall features of particle radial migration is represented by v_f . Due to the non-smooth pressure and velocity distributions, $\min[v_d] \simeq \min[v_f] > 0$ at $-3.5 \lesssim x/H \lesssim -2.5$ and $x/H \sim -2.1$, in addition to $0.0 \lesssim x/H \lesssim 2.0$. It means that all particles have positive radial velocity there and accumulate near the outer edges of these regions. On the other hand, $\max[v_d] \simeq \max[v_f] > 0$ is observed in some areas, for example, around $x/H \simeq 3.0$. A small number of particles are stalled there.

The peaks of particle density at $x/H < 0$ would not grow because there are few particles which can accumulate from outside (Figure 8a). The stagnant areas cannot stall all the particles which migrate inward due to $\min[v_d] < 0$ (Figure 8b). Therefore the peak at $x/H \simeq 2.0$ is the most prominent concentration zone.

Figure 9a shows the time variation of the number of particles in the densest grid in the whole region and at the center of the traced clump. The agreement between the two indicates that the same clump is growing. Figure 9b is the velocity dispersion of particles within the clump at $t = t_c (= 55/\Omega)$. The velocity dispersion is small but is larger than in model- η . While the turbulence does not affect the location of the dust concentration, it does influence the degree of particle accumulation.

When the azimuthal box size is long, shear velocity becomes supersonic near the edge and it may cause artificial density dip (Johnson et al. 2008; Johansen et al. 2009) unless a high-order scheme is applied for Keplerian advection term. To confirm that the density dip found in our simulations is not caused by such a numerical error, we also carried out a run in which the unstable region is put in the side areas and the stable region is at the center. The other parameters are the same as model-s40. We found that the density dip is formed at the side area and no artificial density dip is created in the central area, which means that our numerical scheme using CIP method with the staggered mesh and the short timestep ($dt = 10^{-4}$; Courant condition is set to be < 0.5) is sufficiently high-order scheme.

Let us discuss the effects of a steeper global pressure gradient. Following the same argument as in the final part of section 4.1, from the value of v_f or δu_y , a super-Keplerian region would remain unless the global pressure gradient is as anomalously large as $\beta < -0.64$. To make a more quantitative argument, as was done in Johansen et al. (2007), we also carried out a run with the pressure gradient of $\beta = -0.10$ (model-s40b). The other parameters are the same as model-s40. Figure 10 shows the close-up of the distribution of $\max, \min[v_f]$ and $\max, \min[v_t]$. With the higher negative value of β , gas rotates more slowly and the stronger headwind deprives the dust particles of angular momentum more efficiently to accelerate their inward migration in the sub-Keplerian region. Since v_t does not depend on β , the value

of $|v_f|$ exceeds $|v_t|$ by a larger degree in outer regions. Thus greater amounts of dust particles move to the dust concentration area without becoming locally stagnant due to non-smooth gas pressure and gas velocity fluctuations in the sub-Keplerian region. On the other hand, in the dust concentrated area, the dust particles are affected by turbulence more severely. With more downward shift of the v_f value in the whole region, the dust concentration that occurs at $v_f \simeq 0$ is shifted inward to $x/H \simeq 1.8$ from $x/H \simeq 2.0$. The magnetic turbulence is stronger at this new location and it increases the radial width (δx) of the dust accumulated region (denoted by $\max[v_d] > 0$ and $\min[v_d] < 0$: the gray hatched areas in the figure from $\delta x/H \simeq 0.5$ to $\delta x/H \simeq 0.9$ and doubles the velocity dispersion of particles there. To see the overall consequences of these both positive and negative effects, the number of particles in the most dense grid cell is plotted in Figure 9a together with the result of model-s40. Despite the different dust radial velocity and gas turbulence, the density increase rate and the peak value are only slightly different from each other, although the new run could show higher dust density on longer timescale.

4.2.2. *model-t01*

The effects of turbulence are larger for particles with shorter τ_f . We have run a case with $\tau_f \Omega = 0.1$ (model-t01). Except for the friction time, all the settings are the same as model-s40. Since there is no kick-back from the dust particles to the MHD fluid, MHD results are exactly the same (Figure 6a and Figure 7). The difference in the dust concentration pattern is caused by the enhanced gas drag.

Figure 6c presents the evolution of the particle density. The difference from the previous case that becomes visible at the later time is that the smaller dust particles are scattered over a broader area. Figure 11a shows the radial profile of the dust number density averaged azimuthally and vertically. Since the MHD flow patterns are exactly the same, the prominent density peaks are located at the same position as in model-s40. However, the peak values are lower and the radial widths are wider. Furthermore, more particles stay outside the peaks and are scattered in the stable region.

These differences are caused by the enhanced turbulent diffusion of dust particle motions through enhanced gas drag. Indeed, Figure 11c shows that the turbulent scattering v_t dominates over the steady migration v_f in most areas of the simulation box. Figure 11b shows the estimated radial velocity of particles v_d . The radial velocity of the simulated particles, v_x , are also shown by dots. Although dust particles are swept out of the unstable region, in most parts of the unstable region, $\max[v_d] > 0$ and $\min[v_d] < 0$ are satisfied, so the dust particles are broadly distributed in the stable region with lower concentration.

Nevertheless, identity of the clump with the highest dust concentration is still maintained (Figure 12a). Indeed the velocity dispersion around center of the traced clump shown is not increased significantly (Figure 12b).

We also run a high global pressure gradient model ($\beta = -0.10$). Though the inward migration of dust particles becomes faster on average, the maximum density is unchanged because the remnant turbulence that scatters the dust particles in the dust concentrated region is the dominant factor for this $\tau_f \Omega = 0.1$ case.

4.2.3. *model-s055*

Recent works (e.g., Johansen & Youdin 2007) proposed that turbulence itself concentrates dust particles in turbulent eddies. In their models, lifetime of the eddies has to be longer than the timescale to form dense enough particle clumps for formation of planetesimals. On the other hand, our model proposes another path to accumulate dust particles that turbulence plays a role in transformation of the nearly Keplerian gas flow into the quasi-steady flow with a local rigid rotation region. Because the dust particles accumulate near the outer edge of super-Keplerian parts produced by the rigid rotation and the flow pattern is quasi-steady, the timescale problem does not exist in our model. Actually, in the case of model-s40 and model-t01 with $R_{m,ave} \simeq 0.096$, the same clump with the highest density is maintained until the end of simulations ($t\Omega \simeq 80$).

However, in our model, as $R_{m,ave}$ increases to unity, stronger residual turbulence may destroy the clumps, although the clumps are repeatedly created, which may inhibit planetesimal formation. Here, we examine the cases with larger $R_{m,ave}$ (but still $R_{m,ave} < 1$) to find the critical value of $R_{m,ave}$ for persistent clumping.

In model-s055, the width of the stable region L_s is one eighth of model-s40. Accordingly, $R_{m,ave} = 0.64$ compared to 0.096 of model-s40. Figure 13a shows that the MRI turbulence intrudes into the stable region and covers the whole region without being dissipated. By $t\Omega = 80$, the instability is weakened. Although a clear rigid rotation is not formed inside the unstable region (Figure 14a) because of the stronger turbulence that remains especially in the stable region, the velocity gradient becomes small inside the unstable region and the super-Keplerian zone is formed. As a result, the dust particles are swept out of the unstable region and accumulate near the outer stable/unstable boundary (Figure 13b).

However, because the unstable region occupies larger fraction of the simulation box, the resultant magnetic field diffused out of the unstable region is larger than in the previous models. These lead to stronger remnant turbulence. Figure 15a shows that the number of

particles in the densest grid of the whole region does not agree with that at the center of the traced clump. It means that the clumping is only tentative, although clumps are repeatedly created. The diffusive nature of the clumps in model-s055 is depicted by the larger velocity dispersion shown in Figure 15b.

Thin lines in Figure 15a shows the clump identity test for model-s11 ($R_{m,ave} = 0.37$). It shows that the clumps are not persistent as well. Therefore, we conclude that persistent clumps of dust particles are formed for $R_{m,ave} \lesssim 0.1$.

If the global pressure gradient is steeper, the radial velocity of dust particles is faster and its effect may seem to compete better with that of gas turbulent motion. However, from Figure 14d, the minimum value of v_f becomes negative in the entire regions if $\beta < -0.24$ and no particles can be accumulated at the boundary of super/sub-Keplerian regions. There is not much parameter space where more dust concentration can be expected.

5. Conclusion and Discussion

We have investigated the dust concentration in protoplanetary gas disks that are in the quasi-steady state created by inhomogeneous magnetorotational instability. We set the inhomogeneous instability with the initial radial non-uniformity of either ionization degree or vertical component of the magnetic field. The result of our local three-dimensional resistive MHD simulations with Lagrangian particles clearly shows that the meter or decimeter sized dust particles are concentrated strongly and steadily in either setting except for the cases with $R_{m,ave} > 0.1$ (where $R_{m,ave}$ is the averaged magnetic Reynolds number averaged over the simulation box), which can allow planetesimal formation via gravitational instability.

The MRI growth in our model generates the locally confined super-Keplerian region and this flow is quasi-stable due to the support of gas pressure gradient which is also formed by the MRI. Because unperturbed gas flow is sub-Keplerian due to global pressure gradient, the particles suffering gas drag are concentrated in the Keplerian domain at the outer-edge of the super-Keplerian area. Since the flow is in a quasi-steady state, particles are supplied from outer regions by gas drag migration and the particle density increases significantly.

The process of particle concentration and the increasing rate of dust density depend on the particle size, the initial radial widths of unstable/stable regions, and the initial non-uniformity setting as follows:

The initial non-uniform setting, magnetic field or resistivity: The non-uniform resistivity model produces more stable and clean state of local rigid rotation than the

non-uniform magnetic field model, because the high resistivity dissipates the magnetic perturbations more rapidly in the stable regions. Indeed, the velocity dispersion of particles in clumps is smaller in the non-uniform resistivity model. In the non-uniform magnetic field cases, the magnetic reconnection and the remnant weak instability create less smooth gas velocity field, so that particles tend to assemble at multiple radial positions. On the other hand, in the non-uniform resistivity case, all particles are concentrated at a specific radial position, and the peak values of the particle density in clumps is higher, although the particle density also depends on the size of numerical box.

The dust size, meter or decimeter: The meter-size particles are less coupled with gas motion than decimeter-size ones. Since their radial migration is faster, the meter-sized particles are more likely to be condensed in the radially narrow area without being scattered by the remnant gas turbulence. The peak dust density becomes $\gtrsim 1000$ times larger than the initial value. Even in the decimeter-size particle cases, the velocity dispersion of particles in the clump excited by the remnant turbulence is sufficiently smaller than radial drift velocity due to the quasi-steady gas flow and dust concentration is still observed in the simulations, although the enhanced dust density is at most ~ 100 .

The degree of remnant turbulence: When the stable region is initially smaller in the non-uniform magnetic field model (CASE2), that is, $R_{\text{m,ave}}$ is larger, stronger turbulence tends to remain. For $R_{\text{m,ave}} \lesssim 1$, however, the super-Keplerian area continues to exist and clumps with density ~ 100 times larger than initial values are robustly created. Furthermore, for $R_{\text{m,ave}} \lesssim 0.1$, the clumps are persistent enough for following gravitational instability, while they are tentative and repeatedly produced in the cases of $0.1 \lesssim R_{\text{m,ave}} \lesssim 1$.

We should address the following points in subsequent papers:

consistent magnetic resistivity: We need to calculate the value of magnetic resistivity consistently as a time dependent value, because it is sensitive to both gas and dust densities. Around strong dust concentration areas, gas and dust density become larger and magnetic resistivity becomes higher, which may calm down the remnant turbulence.

Rossby wave instability (RWI): RWI can be caused from a pressure bump on the radial-azimuthal plane. If we simulate in an enlarged box, vortex may grow, although in the non-uniform magnetic field cases, the growth of the instability may be reduced by the azimuthal magnetic field. If RWI occurs, it may serve as a mechanism of dust concentration in the azimuthal direction (Inaba & Barge 2006; Lyra et al. 2008).

the vertical structure of a protoplanetary disk: In the upper disk regions, ionization degree may be so high that the MRI to occur (Fleming & Stone 2003; Fromang & Papaloizou 2006; Oishi et al. 2007). The turbulence there may affect the small dust dynamics near the midplane.

feedback from dust particles onto gas: The feedback may be the most important. A great concentration in our results here will inevitably change gas velocity field and it could affect the condition of dust concentration (density enhancement, velocity dispersion and so on) and planetesimal formation. We have already started simulations with this effect.

collisional destruction: While the velocity dispersions of dust particles in clumps are extremely low in some of our results, the dust particles can be collisionally disrupted into small fragments that are coupled to gas motion and the fragments may be dispersed by even weak turbulence. For clumps to gravitationally collapse, its timescale needs to be smaller than mean collision time. On the other hand, if the dust grains are also produced by the collisions, they might affect the gas ionization state through recombination of electrons onto their surface. We need to address these feedback effects by collisional disruption as well.

We thank the referees for insightful and helpful comments. This work was supported by Grant-in-Aid for JSPS Fellows (208778). The simulations presented in this paper were performed by NEC SX-6 at ISAS/JAXA.

REFERENCES

- Adachi, I., Hayashi, C., & Nakazawa, K. 1976, Prog. Theor. Phys, 56, 1756
- Balbus, S. A., & Hawley, J. F. 1991, ApJ, 376, 214
- Balbus, S. A., & Hawley, J. F. 1998, Reviews of Modern Physics, 70, 1
- Balsara, D. S., Tilley, D. A., Rettig, T., & Brittain, S. A. 2009, MNRAS, 397, 24
- Barge, P., & Sommeria, J. 1996, A&A, 295, 1
- Chiang, E. I., & Murray-Cley, R. A. 2007, Nature Phys., 3, 604
- Cuzzi, J. N., Dobrovolskis, A. R., & Champney, J. M. 1993, Icarus, 106, 102

- Dubrulle, B., Morfill, G., & Sterzik, M. 1995, *Icarus*, 114, 237
- Fleming, T. P., Stone, J. M., & Hawley, J. F. 2000, *ApJ*, 530, 464
- Fleming, T., & Stone, J. M. 2003, *ApJ*, 585, 908
- Fromang, S., & Papaloizou, J. 2006, *A&A*, 452, 751
- Gammie, C. F. 1996, *ApJ*, 457, 355
- Glassgold, A. E., Najita, J., & Igea, J. 1997, *ApJ*, 480, 344
- Goldreich, P., & Ward, W. R. 1973, *ApJ*, 183, 1051
- Gomez, G. C., & Ostriker, E. C. 2005, *ApJ*, 630, 1093
- Goodman, J., & Pindor, B. 2000, *Icarus*, 148, 537
- Hayashi, C., 1981, *Prog. Theor. Phys. Suppl.* 70, 35
- Hawley, J. F., Gammie, C. F., & Balbus, S. A. 1995, *ApJ*, 440, 742
- Igea, J., & Glassgold, A. E. 1999, *ApJ*, 518, 848
- Ilgner, M., & Nelson, R. P. 2008, *A&A*, 483, 815
- Inaba, S., & Barge, P. 2006, *ApJ*, 649, 415
- Ishitsu, N., & Sekiya, M. 2003, *Icarus*, 148, 537
- Jin, L. 1996, *ApJ*, 457, 798
- Johansen, A., Klahr, H., & Henning, Th. 2006a, *ApJ*, 636, 1121
- Johansen, A., Henning, T., & Klahr, H. 2006b, *ApJ*, 643, 1219
- Johansen, A., & Youdin, A. N. 2007, *ApJ*, 662, 627
- Johansen, A., Oishi, J. S., Mac Low, M.-M., Klahr, H., Henning, Th., & Youdin, A. 2007, *Nature*, 448, 1022
- Johansen, A., Youdin, A., & Klahr, H. 2009, *ApJ*, 697, 1269
- Johnson, B. M., Guan, X., & Gammie, C. F. 2008, *ApJS*, 177, 373
- Kato, T. M., Nakamura, K., Tandokoro, R., Fujimoto, M., & Ida, S. 2009, *ApJ*, 691, 1697 (Paper I)

- Li, H., Colgate, S. A., Wendroff, B., & Liska, R. 2001, *ApJ*, 551, 874
- Lyra, W., Johansen, A., Klahr, H., & Piskunov, N. 2008, *A&A*, 491, L41
- Miyake, K., & Nakagawa, Y. 1995, *ApJ*, 441, 361
- Nakagawa, Y., Sekiya, M., & Hayashi, C. 1986, *Icarus*, 115, 304
- Oishi, J. S., Mac Low, M-M., & Menou, K. 2007, *ApJ*, 670, 805
- Papaloizou, J. C. B., & Terquem, C. 1997, *MNRAS*, 287, 771
- Pneuman, G. W., & Mitchell, T. P. 1965, *Icarus*, 4, 494
- Safronov, V. S. 1969, *Evolution of the Protoplanetary Cloud and the Planets*, NASA Tech. Transl. F-677
- Sano, T., Inutsuka, S., & Miyama, S. M. 1998, *ApJ*, 506, L57
- Sano, T., & Miyama, S. M. 1999, *ApJ*, 515, 776
- Sano, T., Miyama, S. M., Umebayashi, T., & Nakano, T. 2000, *ApJ*, 543, 486
- Stone, J. M., & Norman, M. L. 1992a, *ApJS*, 80, 753, 1992b, *ApJS*, 80, 791
- Umebayashi, T. 1983, *Prog. Theor. Phys.*, 69, 480
- Varniere, P., & Tagger, M. 2006, *A&A*, 446, L13
- Wardle, M., & Ng, C. 1999, *MNRAS*, 303, 239
- Weidenschilling, S. J. 1977, *MNRAS*, 180, 57
- Weidenschilling, S. J. 1980, *Icarus*, 44, 172
- Wisdom, J., & Tremaine, S. 1988, *AJ*, 95, 925
- Yabe, T., & Aoki, T. 1991, *Comput. Phys. Comm.*, 66, 219
- Youdin, A. N., & Goodman, J. 2005, *ApJ*, 662, 613
- Youdin, A. N., & Johansen, A. 2007, *ApJ*, 662, 613

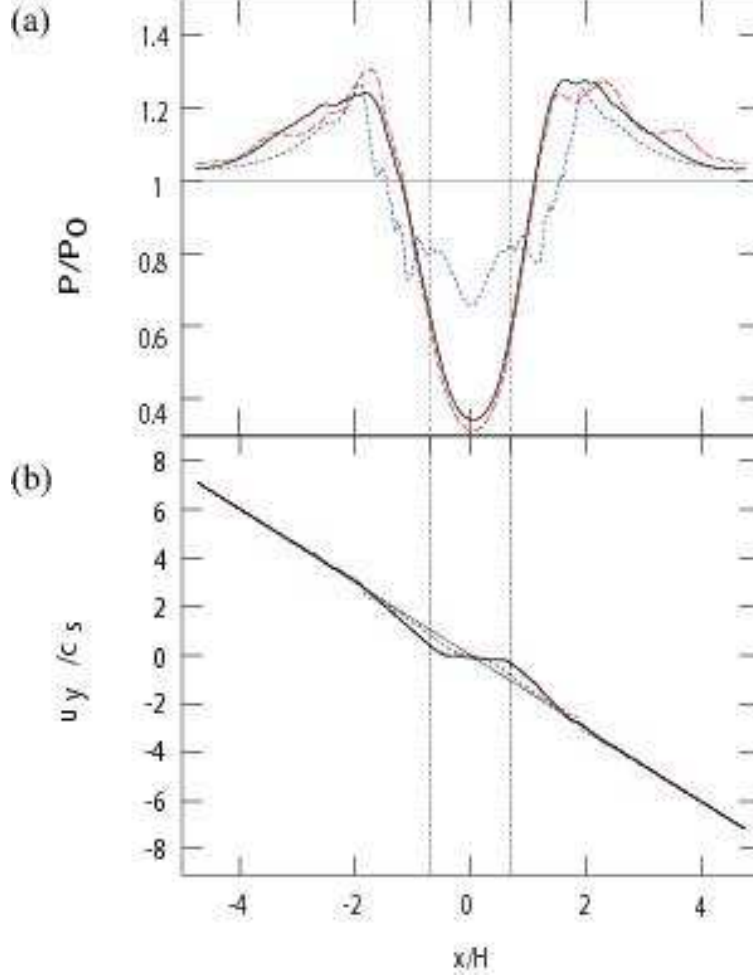


Fig. 1.— Results of the two-dimensional version of model-s40 ($dB_z(t=0)/dx \neq 0$, $L_s/H = 4.0$) described in Paper I. The corresponding result of the three-dimensional simulation is shown in Fig. 7. Time evolution of vertically averaged values of (a) pressure P and (b) gas angular velocity u_y . The thin solid, dotted, dashed and bold lines are the snapshots at $t\Omega = 0, 27, 40$ and 70 , respectively. The two vertical dotted-lines are the boundaries between the unstable and stable regions. MRI is initially excited only between the two dotted lines.

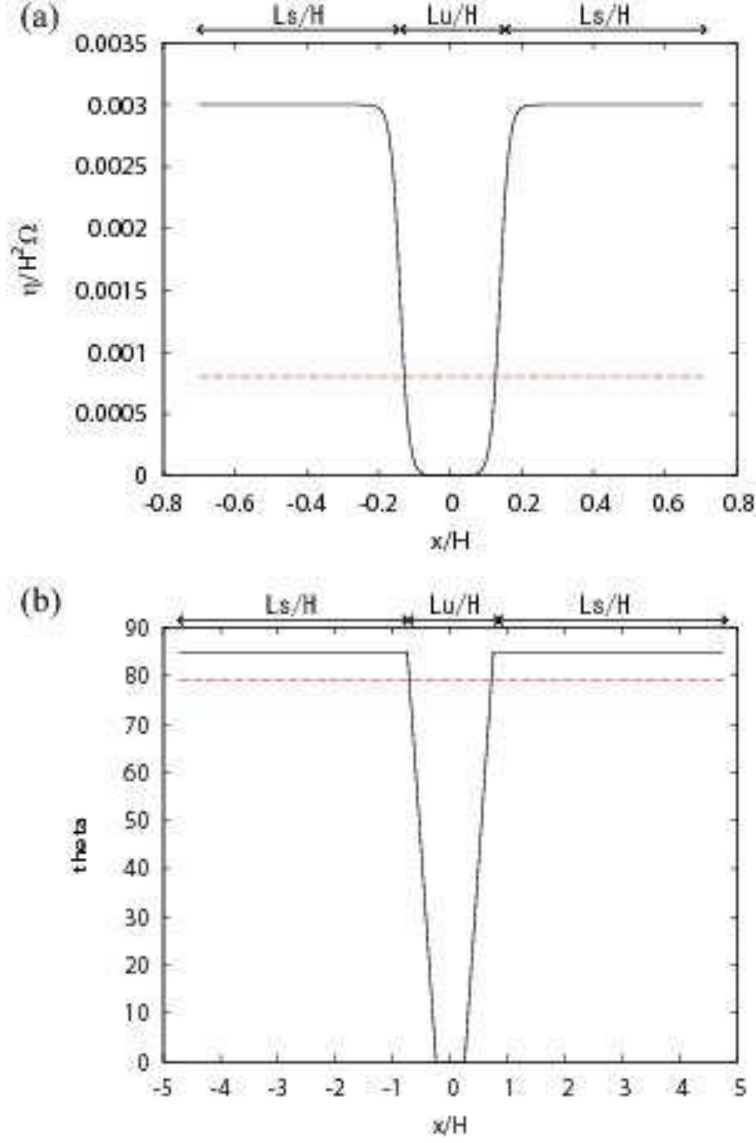


Fig. 2.— Two versions of initial setting to realize the non-uniform MRI growth in the simulation box. (a) The non-uniform radial distribution of resistivity used in CASE1 (model- η), where the dashed line represents the critical value for MRI development predicted by the linear theory. (b) The non-uniform radial distribution of the magnetic field angle θ in CASE2 (model-s40), where the dashed line shows the critical angle for MRI predicted by the linear theory (for detail, see Paper I).

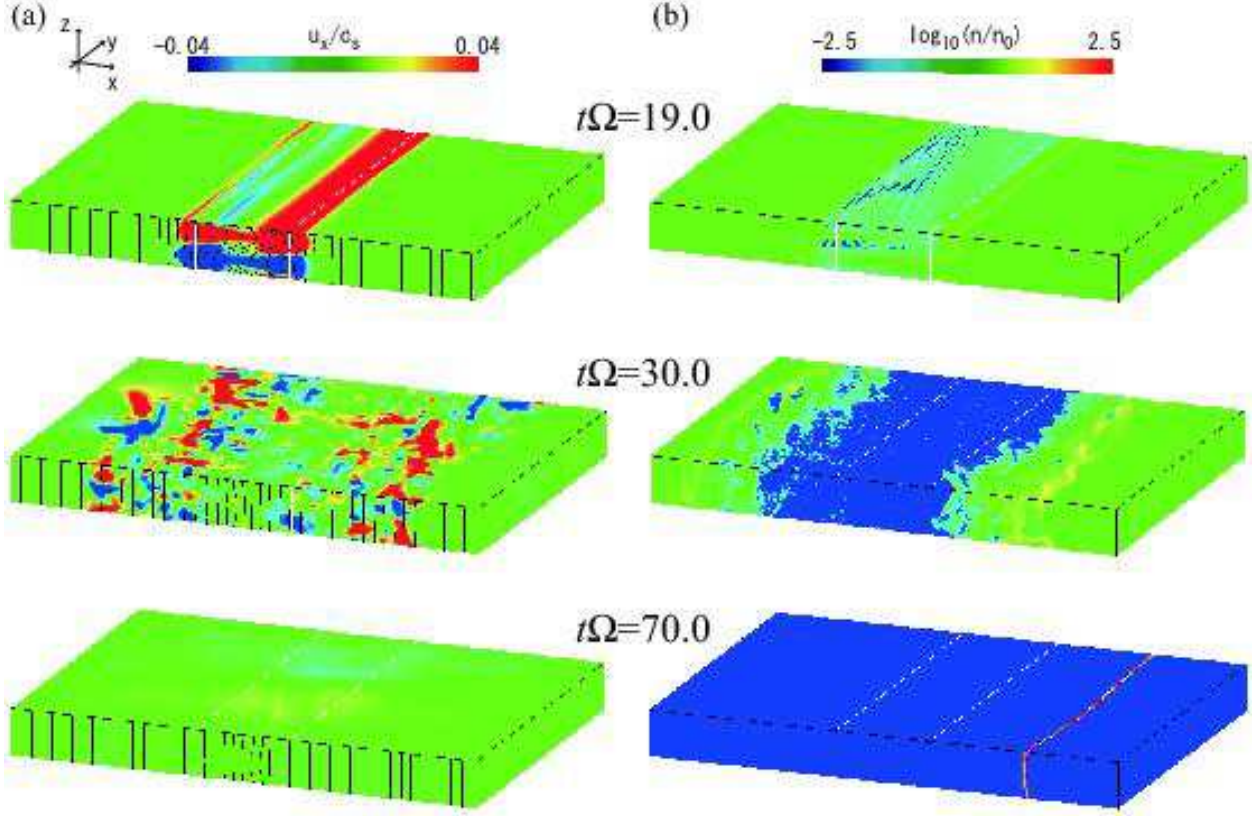


Fig. 3.— The results of model- η ($d\eta/dx \neq 0$, $\tau_f\Omega = 1.0$). (a) Time evolution of the magnetic field (black lines) and the angular velocity u_y (contours) of gas. (b) Particle density normalized by the initial value. The unstable region is between the two white lines. Non-uniform growth of MRI and its relaxation seen in Panel a lead to the dust concentration depicted in Panel b.

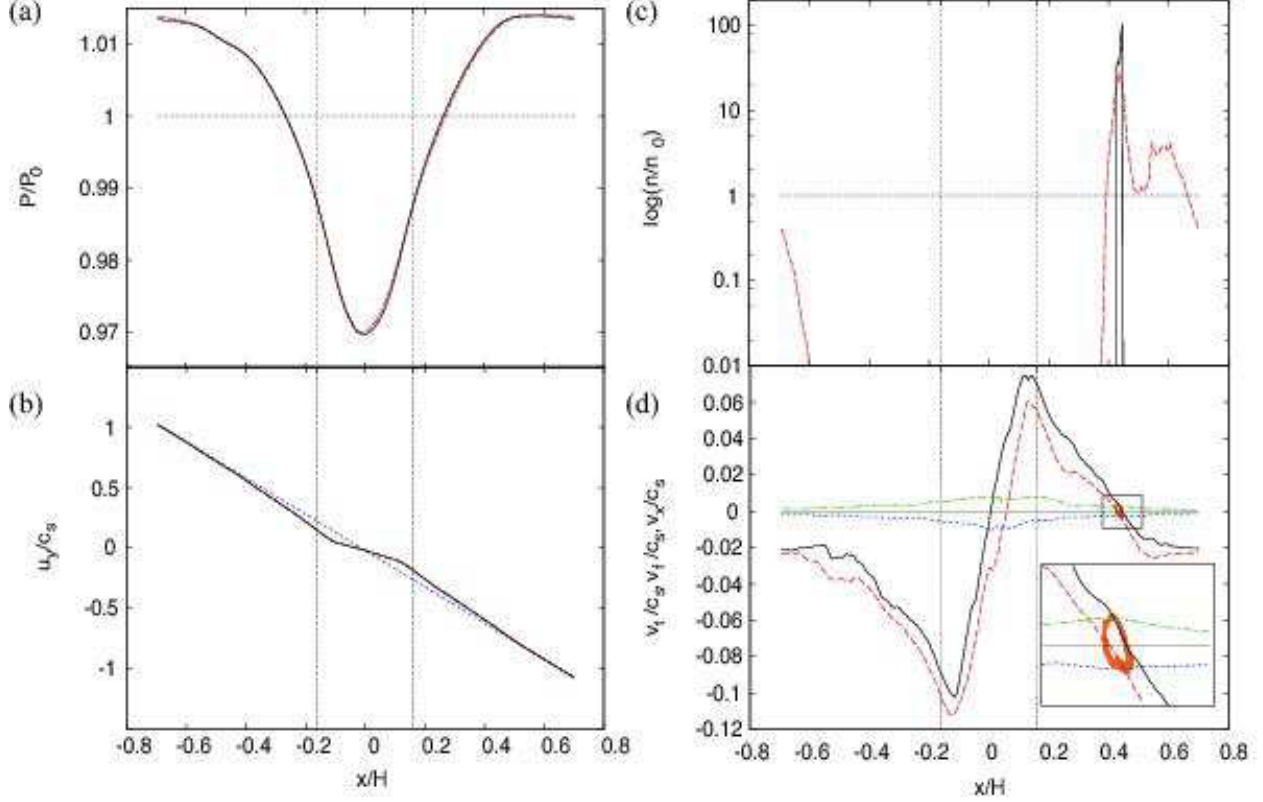


Fig. 4.— Radial dependences of (a) pressure P , (b) gas angular velocity u_y , (c) the number of particles normalized by the initial value, and (d) the maximum and minimum values of v_f and v_t and the actual particle radial velocity $v_{x,i}$, in model- η ($d\eta/dx \neq 0, \tau_f\Omega = 1.0$). They are averaged both azimuthally and vertically. In Panels a, b and c, the dotted, dashed, and solid lines represent the results at $t\Omega = 0, 40$ and 70 , respectively. Since v_f is predicted by equation (13) using simulated gas velocity after the establishment of the quasi-steady flow ($t\Omega = 70$) and the simulated gas velocity has a component of turbulence, it has the maximum (the solid line) and minimum (the dashed line) values as shown in Panel d. In Panel d, the maximum/minimum values of v_t and the actual particle velocity are also plotted by dash-dotted/dotted lines and dots.

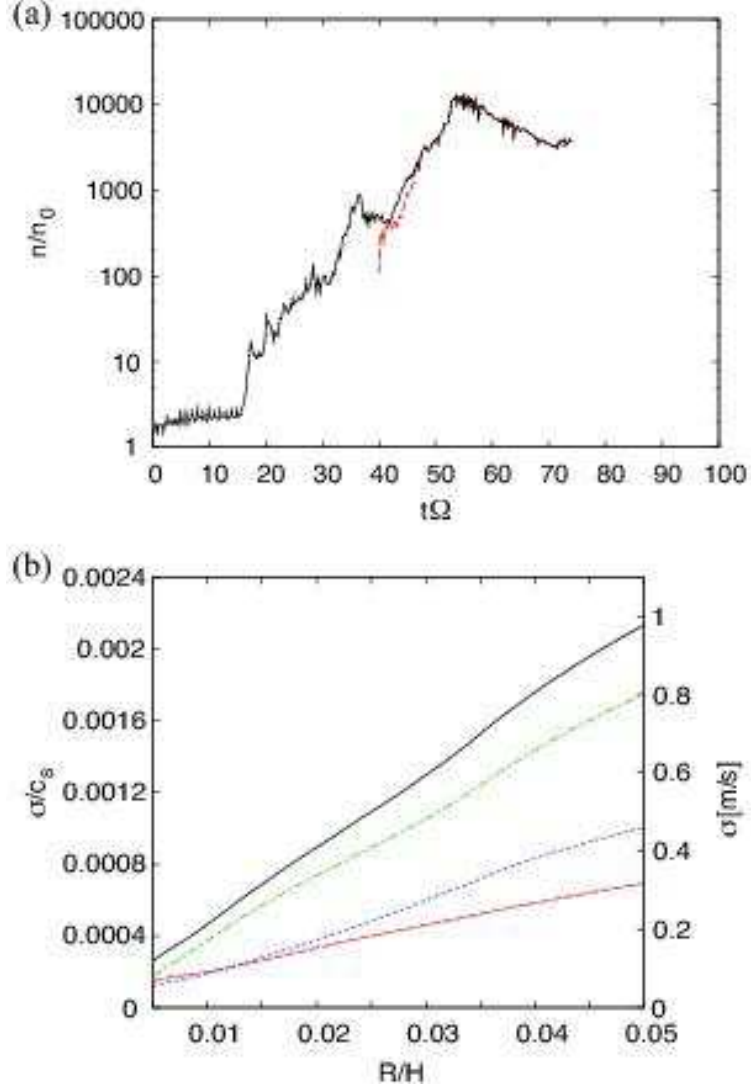


Fig. 5.— Time evolution of dust concentration in model- η ($d\eta/dx \neq 0$, $\tau_f\Omega = 1.0$). (a) The solid line represents the number of particles in the cell having the highest density in the whole region, which is normalized by the initial value, while the dashed line is the number of particles in the cell at the center of the traced clump. (b) Velocity dispersion in the traced clump at $t\Omega = t_c\Omega$ ($=55.0$ in this case). The solid, dashed, dash-dotted and dotted lines show total, radial, azimuthal and vertical components, respectively. The sound velocity is estimated as 500 m/s with temperature $T \simeq 70K$ at 5AU.

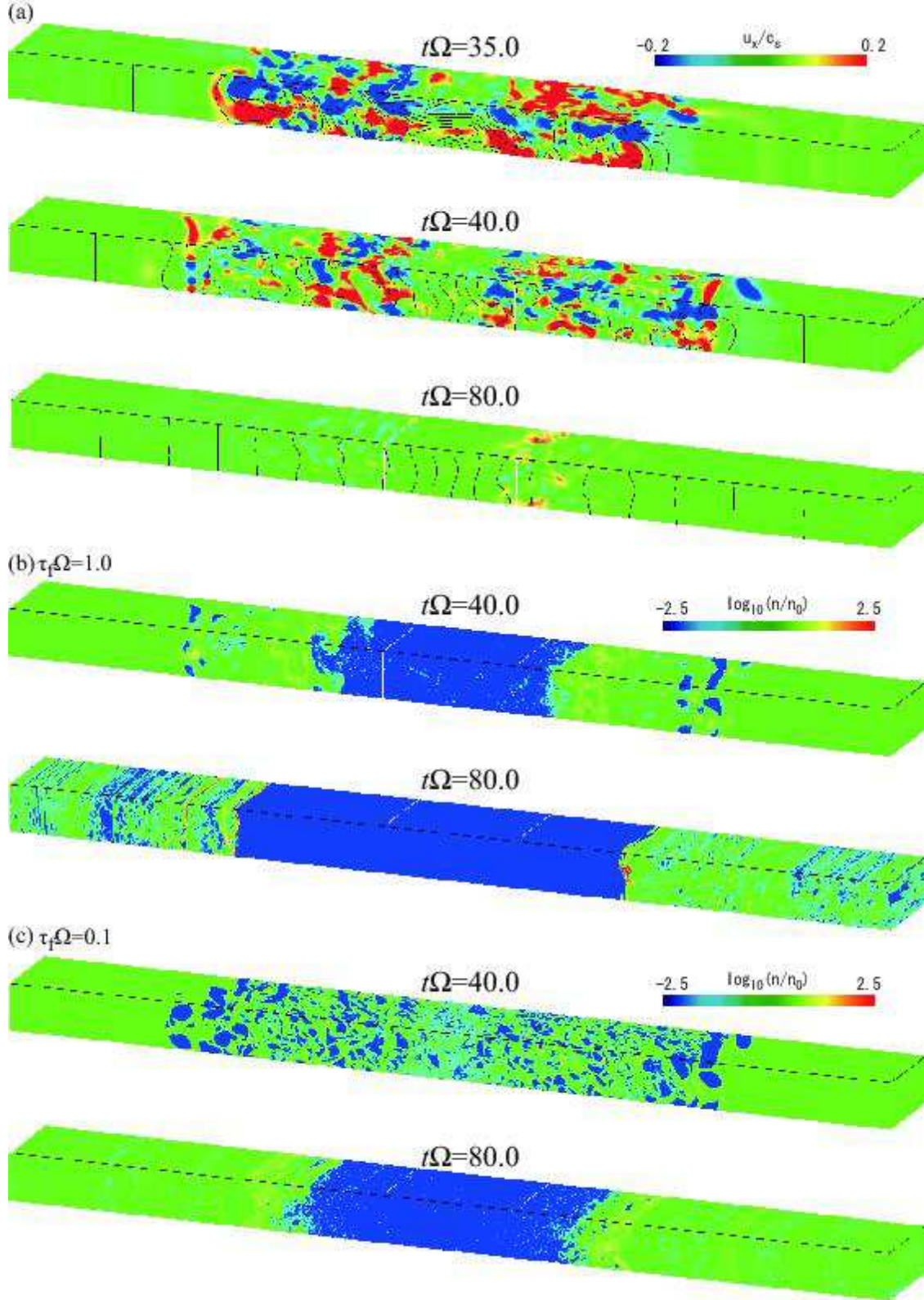


Fig. 6.— (a)(b) The same as Figure 3 but for model-s40 ($dB_z(t=0)/dx \neq 0, L_s/H = 4.0, \tau_f\Omega = 1.0$). (c) Particle density distribution for model-t01 ($\tau_f\Omega = 0.1$).

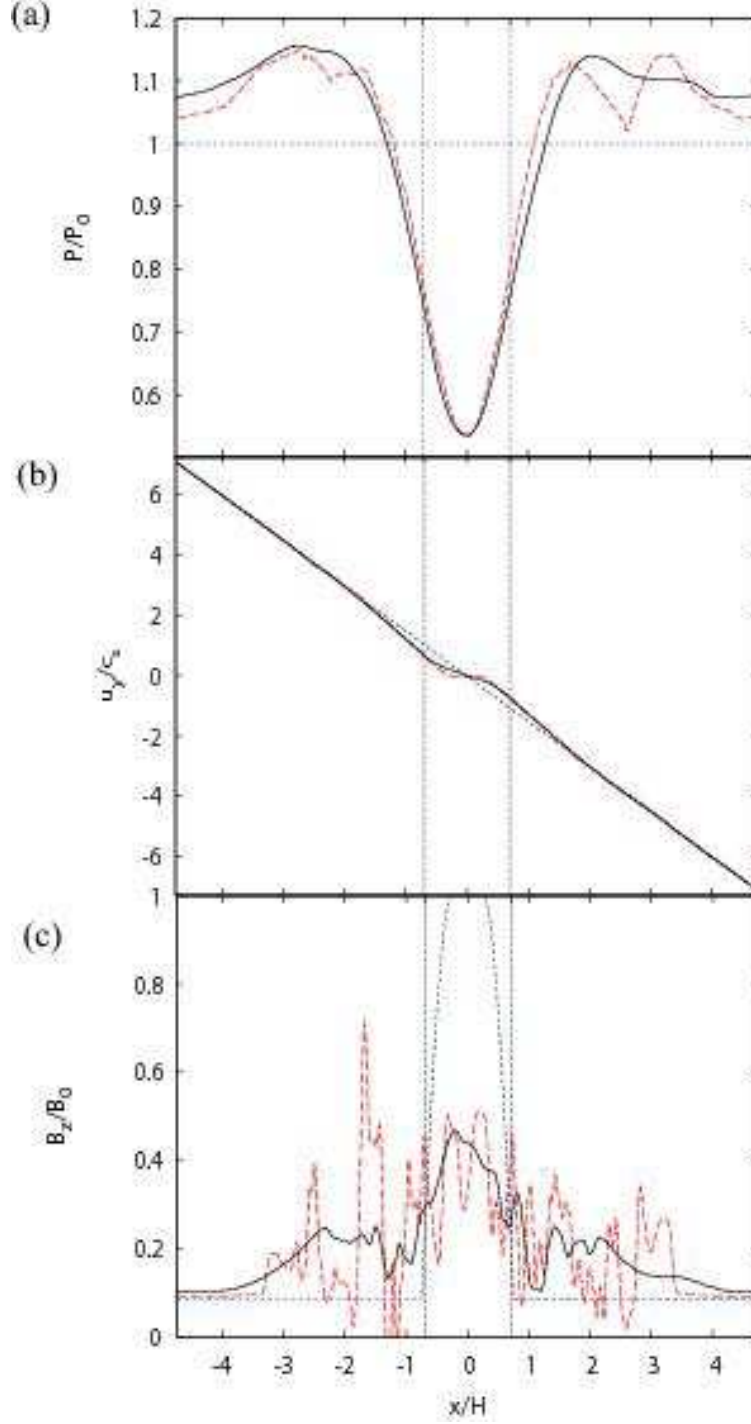


Fig. 7.— Time evolution of azimuthally and vertically averaged values of (a) pressure P , (b) gas angular velocity u_y , and (c) vertical magnetic component B_z , for model-s40 and model-t01 ($L_s/H = 4.0$). The dotted, dashed and bold lines represent the snapshots at $t\Omega = 0, 40$ and 70 , respectively.

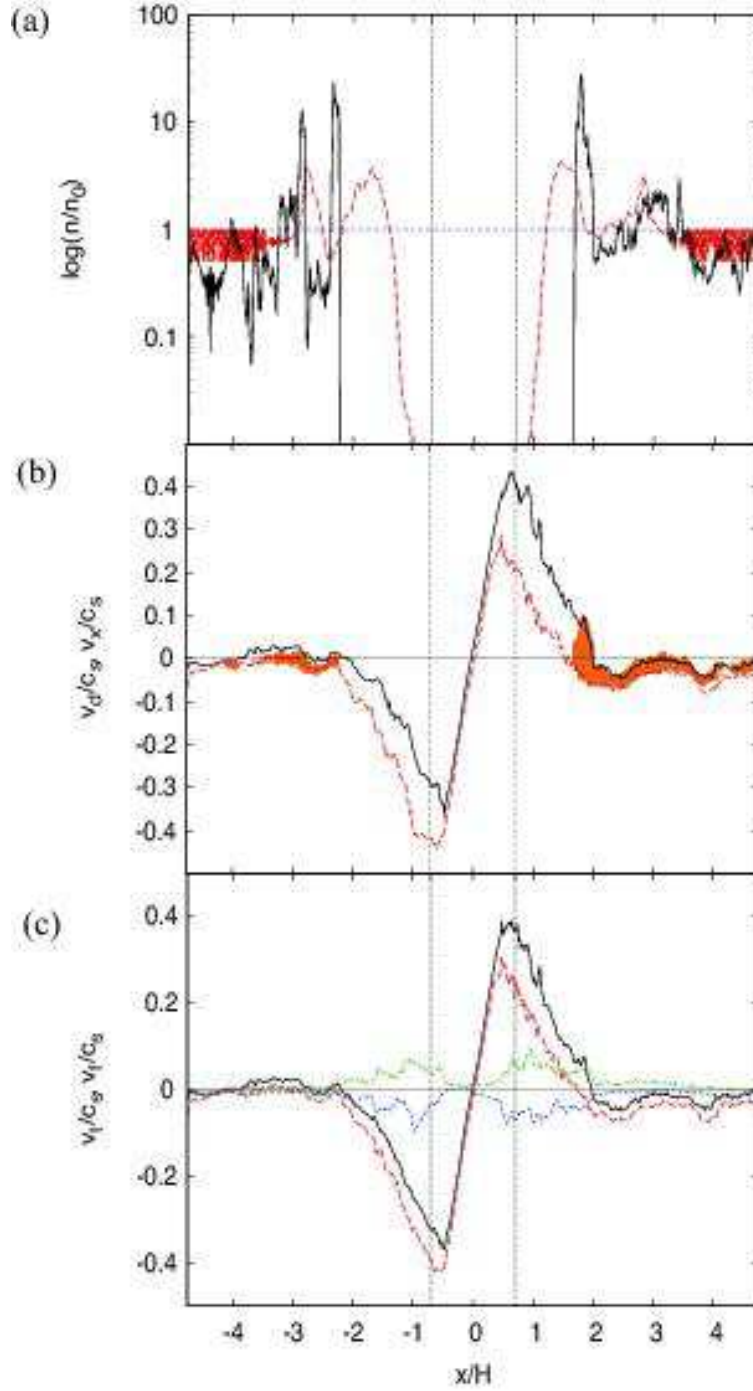


Fig. 8.— Dust concentration in model-s40 ($L_s/H = 4.0, \tau_f\Omega = 1.0$). (a) Time evolution of the number of particles in each radial grid scaled by the initial value, where the dotted, dashed and bold lines represent the snapshots at $t\Omega = 0, 40$ and 70 , respectively. (b) Radial velocity of particle v_x (dots) and the estimated radial velocity v_d that are azimuthally and vertically averaged, where the solid and dashed lines express the maximum and minimum values in the averaging, respectively. (c) v_t (max: bold solid, min: bold dashed) and max/min of v_t (thin lines). The results in Panels b and c are obtained at $t\Omega = 70$.

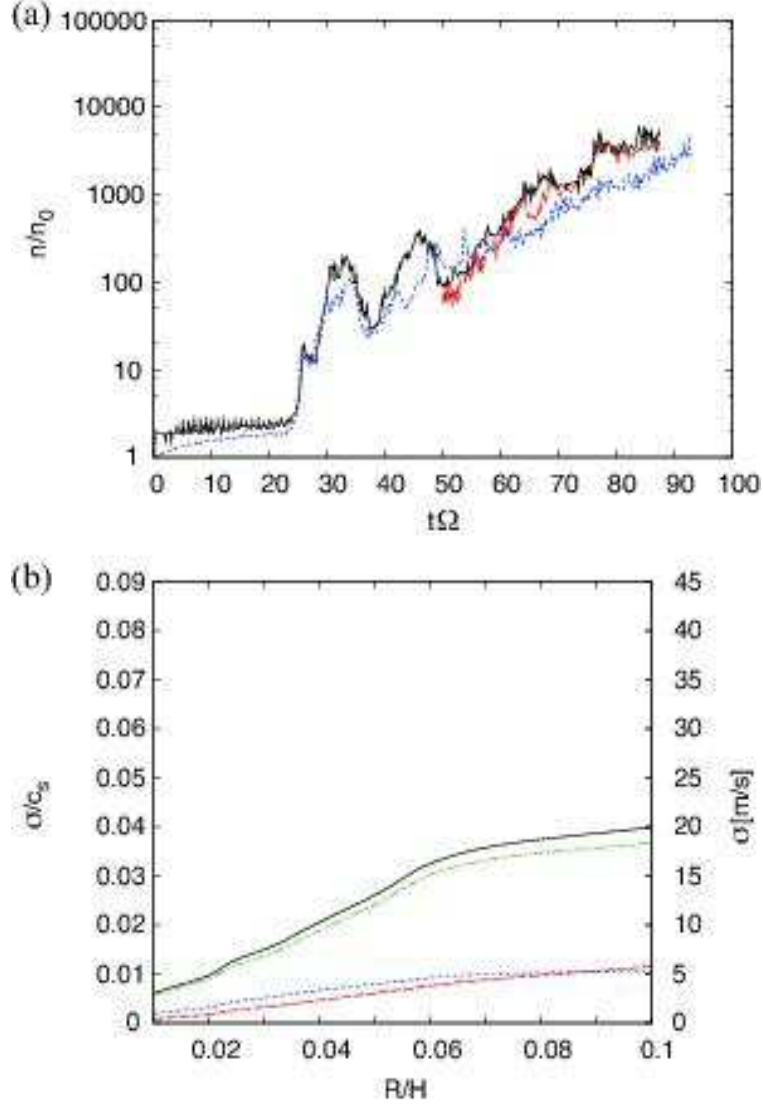


Fig. 9.— The same plots as Figure 5 but for model-s40 ($L_s/H = 4.0$, $\tau_f\Omega = 1.0$, $\beta = -0.04$). The dotted line in Panel a is the number of particles in the densest cell in model-s40b ($\beta = -0.10$).

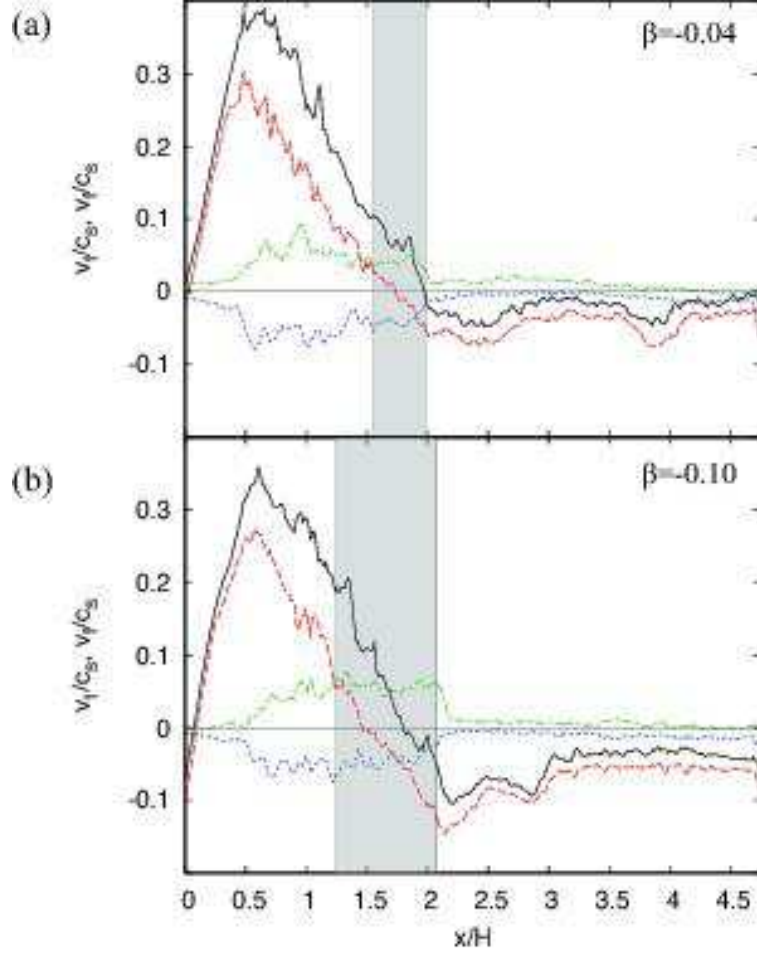


Fig. 10.— (a) The closeup of Figure 8c (model-s40 in which $\beta = -0.04$). (b) The same plots with Panel a but for model-s40b in which $\beta = -0.10$.

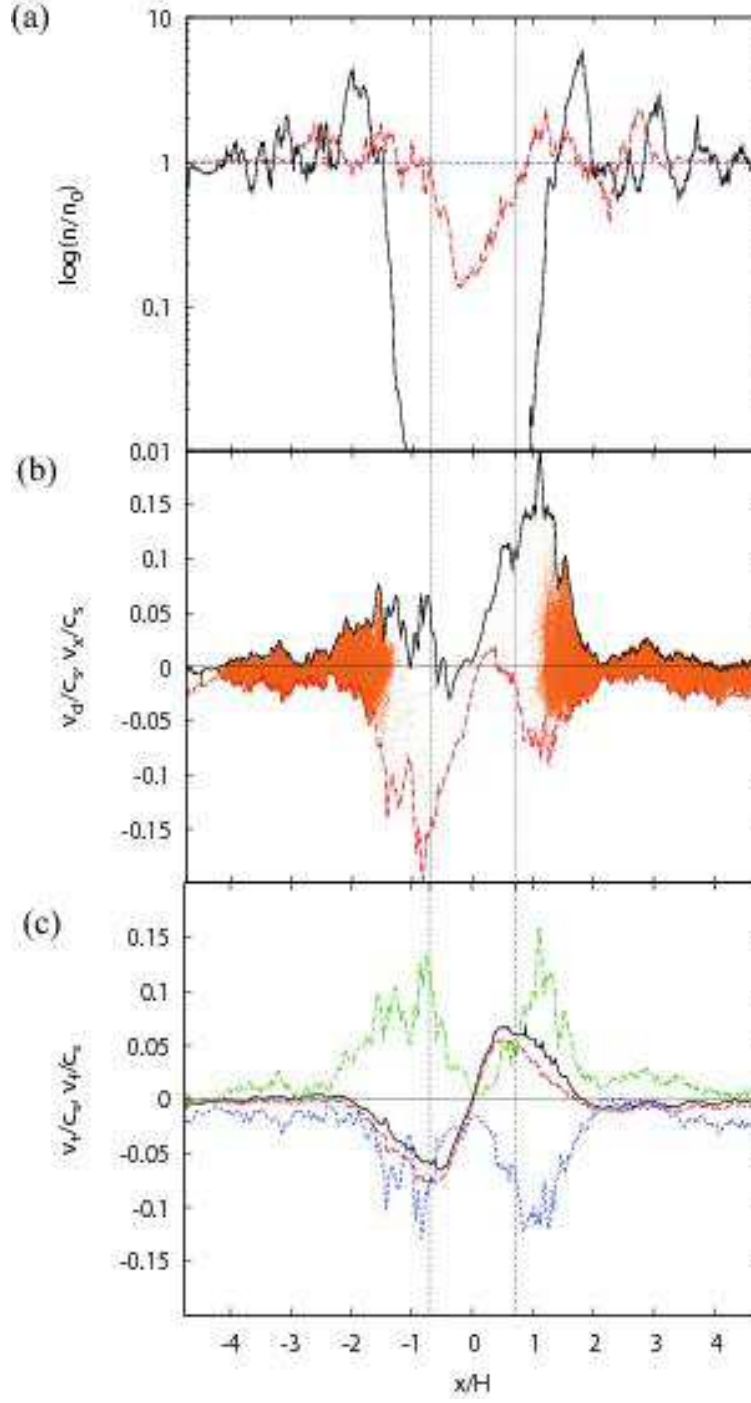


Fig. 11.— The same plots as Figure 8 but for model-t01 ($L_s/H = 4.0, \tau_f\Omega = 0.1$), where turbulence effects are enhanced.

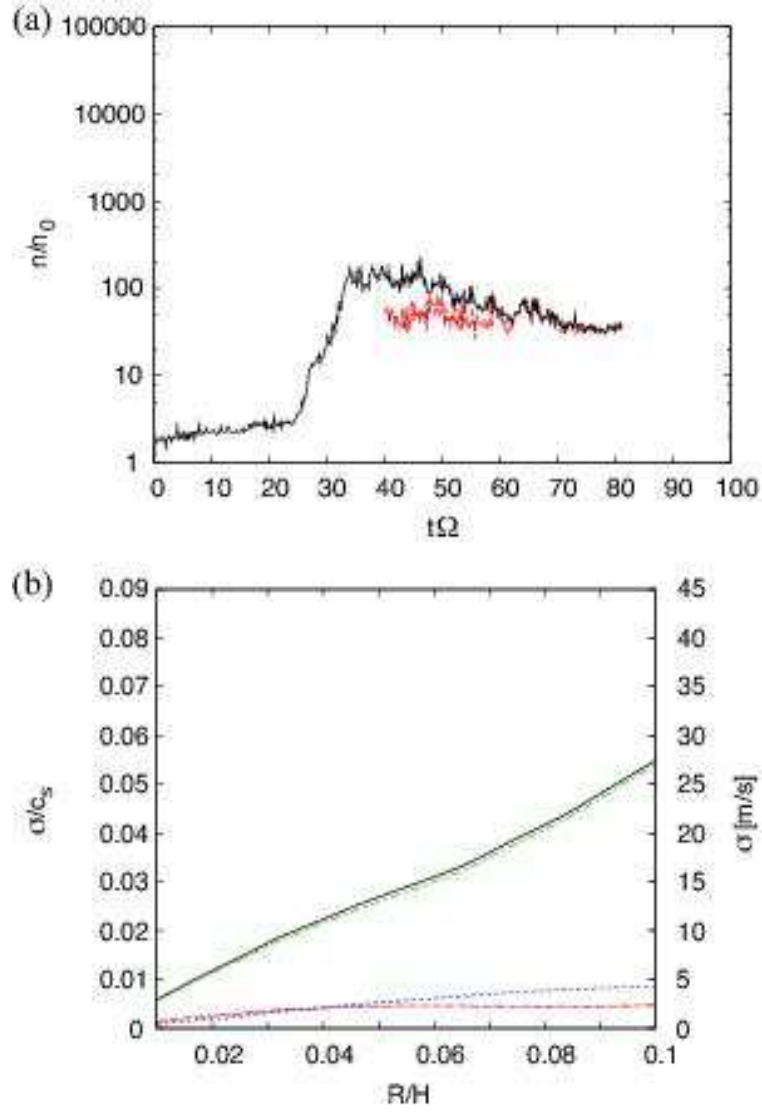


Fig. 12.— The same plots as Figure 5 but for model-t01 ($L_s/H = 4.0$, $\tau_f\Omega = 0.1$).

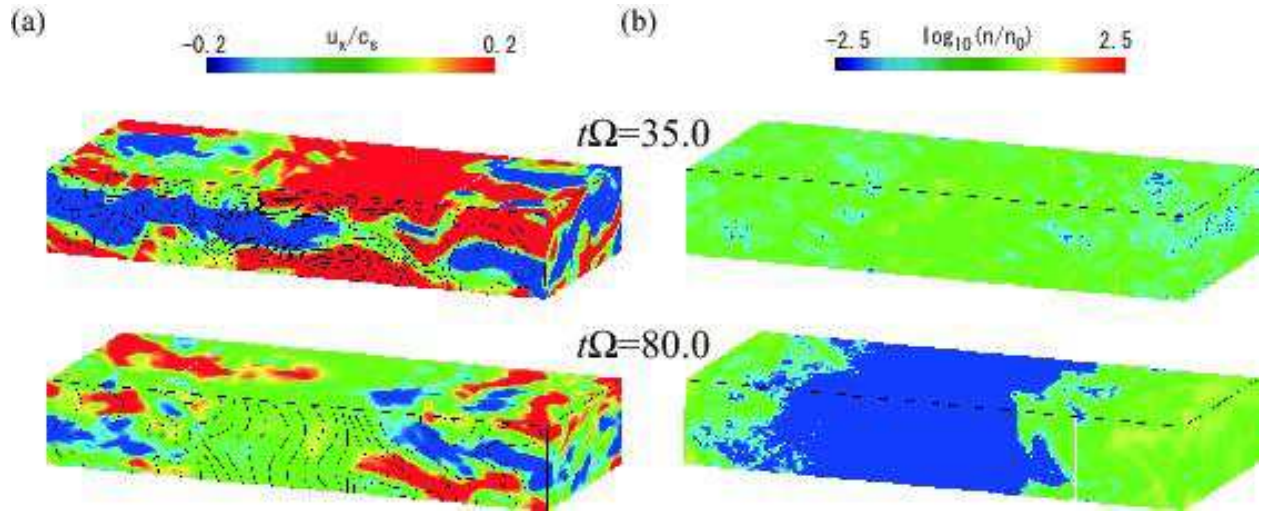


Fig. 13.— The same plots as Figure 3 but for model-s055 ($L_s/H = 0.55$, $\tau_f\Omega = 1.0$).

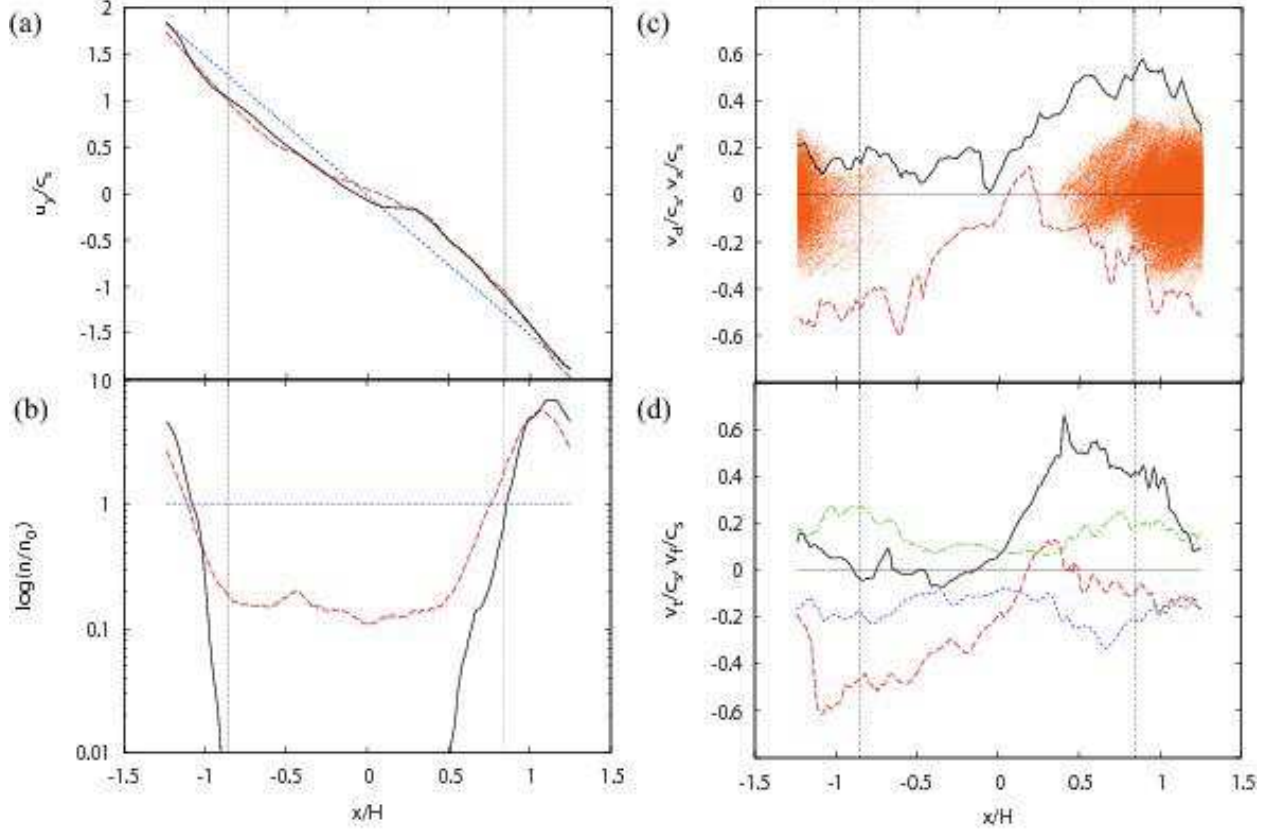


Fig. 14.— (a) Time evolution of both azimuthally and vertically averaged angular velocity of gas u_y in model-s055 ($L_s/H = 0.55, \tau_f\Omega = 1.0$), where the dotted, dashed and bold lines represent the snapshots at $t\Omega = 0, 40$ and 70 , respectively. (b)(c)(d) The same plots as Figure 8a, b, and c but for model-s055. Dust particles are scattered due to elevated turbulence.

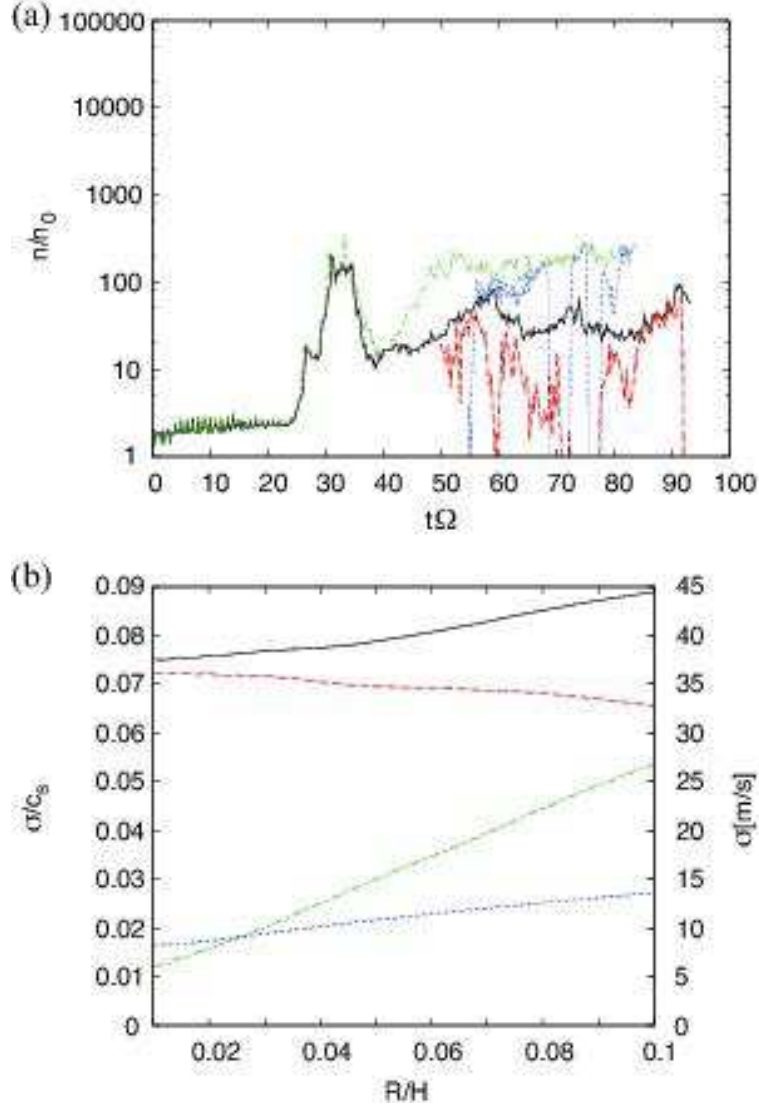


Fig. 15.— The same plots as Figure 5 but for model-s055 ($L_s/H = 0.55, \tau_f\Omega = 1.0$). The thin dash-dotted and thin dotted lines in Panel a show the results of model-s011 ($L_s/H = 1.1, \tau_f\Omega = 1.0$).

model-	$L_x \times L_y \times L_z (/H)$	$N_x \times N_y \times N_z$	non-uniform parameter	L_u/H	L_s/H	$R_{m,ave}$	$\tau_f \Omega$	$N_d/10^7$
η	$1.4 \times 1.0 \times 0.14$	$280 \times 200 \times 28$	η	0.28	0.56	***	1.0	1.3
s40	$9.5 \times 1.0 \times 0.50$	$950 \times 100 \times 50$	B	1.4	4.0	0.096	1.0	3.8
s11	$3.5 \times 1.0 \times 0.50$	$350 \times 100 \times 50$	B	1.4	1.1	0.37	1.0	1.4
s055	$2.5 \times 1.0 \times 0.50$	$250 \times 100 \times 50$	B	1.4	0.55	0.64	1.0	1.0
t01	$9.5 \times 1.0 \times 0.50$	$950 \times 100 \times 50$	B	1.4	4.0	0.096	0.1	3.8

Table 1: RUN PARAMETERS (1): Name of run. (2): Size of simulation box. (3): Grid resolution. (4): Parameter set non-uniformly. (5): Radial width of unstable region. (6): Radial width of stable region. (7): Friction time. (8): Number of particles.

model-	$t_c \Omega$	$\Omega \delta t_{trace}$	N_c	$\sigma_{p,ave} (\sigma_{p,x}, \sigma_{p,y}, \sigma_{p,z}) / H$
η	55.0	34.0	71096	0.013(0.0023, 0.012, 0.0036)
s40	75.0	37.4	13823	0.16(0.041, 0.14, 0.054)
s11	75.0	33.6	2285	0.77(0.67, 0.24, 0.13)
s055	90.0	43.2	392	0.65(0.57, 0.24, 0.13)
t01	75.0	41.2	292	0.18(0.086, 0.13, 0.069)

Table 2: TRACED PARTICLES (1): Name of run. (2):Time to define which particles are traced. (3): Period for tracing. (4): Number of traced particles. (5): Position dispersion of N_c particles averaged for $\delta t_{trace} \Omega$ and its composition.